Digital programming of reciprocity breaking in resonant piezoelectric metamaterials

Mustafa Alshaqaq [1,*] Christopher Sugino [2] and Alper Erturk [1]
[1]*G.W. Woodruff School of Mechanical Engineering, Georgia Institute of Technology, Atlanta, Georgia 30332, USA*
[2]*Department of Mechanical Engineering, Stevens Institute of Technology, Hoboken, New Jersey 07030, USA*

(Received 15 March 2023; accepted 8 September 2023; published 2 October 2023)

We demonstrate a digitally controlled piezoelectric metamaterial waveguide leveraging resonant, spatiotemporally modulated synthetic impedance circuits for programmable reciprocity breaking. Piezoelectric metamaterials have effective stiffness that depends on the shunt circuitry connected to each unit cell, offering greatly increased design freedom over their purely mechanical counterparts. By connecting a digitally controlled synthetic impedance shunt circuit to each unit cell of the metamaterial domain, the effective stiffness is externally programmed according to a desired profile in space and time. Specifically, we present threefold capabilities in this electromechanical system: (1) smooth parameter modulation (no abrupt switching) through synthetic impedance circuits that eliminate cumbersome analog electrical components, (2) resonant electromechanical modulation in space and time so that one does not have to operate near the Bragg band gap, and (3) precise digital programming by numerically entering the space and time properties of the domain. We also demonstrate the frequency conversion in narrow-band excitation centered at a directional band gap. The experimental results are compared against high-fidelity multiphysics finite-element simulations, yielding excellent agreement for this class of digitally programmable nonreciprocal elastic metamaterials.

DOI: 10.1103/PhysRevResearch.5.043003

I. INTRODUCTION

Conventional media with linear time-invariant material properties allow waves to propagate symmetrically in space from one point to another, as a fundamental law in electromagnetics and acoustics known as the law of reciprocity [1,2]. Because of this inherent reciprocity, using linear time-invariant systems and materials to achieve transmission in one direction is impossible. Yet, the idea of breaking reciprocity in elastic and acoustic systems is of great interest in science and engineering [3,4] as it enables many potential applications in wave control [5]. The objective of achieving unidirectional wave propagation by breaking reciprocity has attracted researchers' attention and opened different research directions. Some of these research areas include investigations of propagating waves in acoustic and elastic media comprising (i) moving parts [6–9], (ii) nonlinearities [10–21], and (iii) time-varying properties [22–31]. Under each of these general research areas, there are several approaches to break the reciprocity of acoustic and elastic waves. Examples include a moving fluid with constant speed which enables reciprocity breaking in acoustic media [8], use of a linear elastic phononic crystal followed by a nonlinear one [32], and modulating the media properties in space and time by coupling membranes to external electromagnetic fields in acoustic metamaterials to dynamically modulate the acoustic impedance [33] or by coupling the elastic media with, for example, piezoelectric elements [34] and magnetic electrical coil elements [35]. These approaches share similarities with recent work on active metamaterials, which use smart or active components to vary and/or enhance the effective material properties of a metamaterial [36–40].

Space-time (or spatiotemporally) modulated linear systems are an effective platform to break wave reciprocity. For example, Trainiti and Ruzzene [23] numerically studied wave propagation in space-time modulated rods and beams in which modulation is performed on the density of the structures, reporting the appearance of unidirectional band gaps in the dispersion relations. Nassar *et al.* [26] analyzed resonant mass-in-mass discrete systems by modulating the inner stiffness of the unit cells in space and time, showing nonreciprocal wave propagation. Sugino *et al.* [41] presented a generalized plane-wave-expansion-based computational framework for piezoelectric shunt circuit strategies in nonreciprocal wave propagation by taking into consideration continuous modulation of circuit parameters.

The first experimental realization [42] of a nonreciprocal acoustic metamaterial used a mass-spring chain of repelling magnets controlled by a modulated array of electromagnets. In another work, Chen *et al.* [35] designed an elastic beam with embedded magnets coupled to adjacent electrical coils in which the ac current is modulated in space and time. Spatiotemporal modulation in conventional elastic structures is challenging to realize experimentally without complex designs. This has led researchers to explore piezoelectric metamaterials as means for demonstrating

*mshaqaq3@gatech.edu

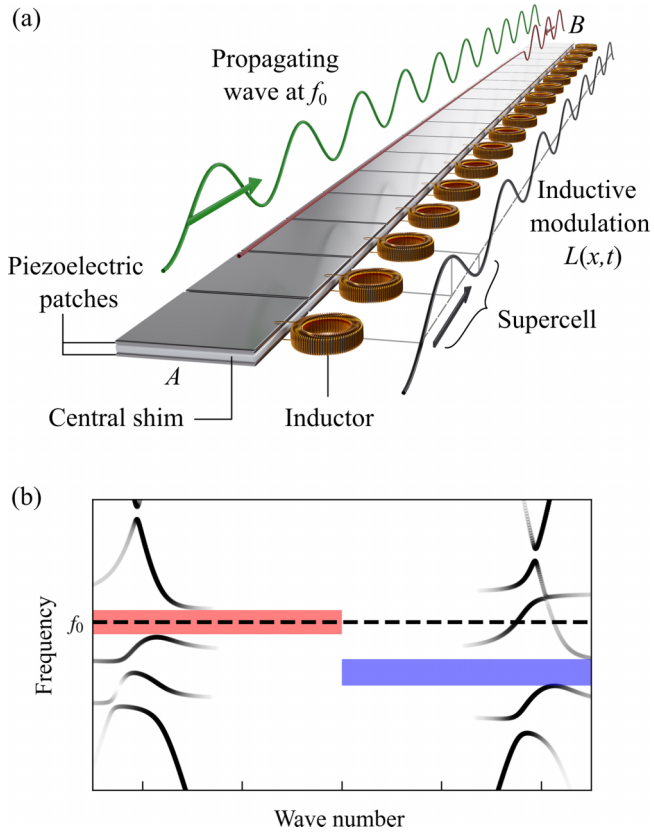

FIG. 1. Nonreciprocal propagation of elastic waves in a piezoelectric metamaterial by smooth parameter variation in space and time. (a) Schematic illustration of a spatiotemporally modulated piezoelectric metamaterial enabled by varying the inductance in space and time in a wavelike fashion. At frequency f_0, transmission from A to B is possible, but no transmission from B to A. (b) The band structure is obtained by using the plane-wave expansion method (cf. Appendix A).

reciprocity breaking in elastic media. Marconi *et al.* [34] used piezoelectric elements shunted to analog negative capacitance circuits to modulate the effective stiffness of the elastic medium via switching logic, and observed reciprocity breaking. Both constructing and tuning analog circuits on a breadboard can be cumbersome, and smooth variation of material properties is not possible using switching circuits. In this paper, we demonstrate a class of nonreciprocal piezoelectric metamaterials with digital control through numerical simulations and experiments. Specifically, we demonstrate spatiotemporal modulation of resonant (inductive) shunts for substantial tunability, enabled by synthetic impedance circuits [43] for precise programming and smooth parameter variation unlike analog circuits with switches. Finite-element simulations are performed to guide the experiments, and the numerical results are validated through detailed comparisons.

II. RESULTS

A. Piezoelectric metamaterial and experiments

Figure 1(a) shows a schematic illustration of a nonreciprocal piezoelectric metamaterial domain with unit cells connected to inductive shunts. Upon varying the inductance values in a wavelike fashion, directional band gaps open permitting waves at frequency f_0 to propagate in one direction as shown by the dispersion relation in Fig. 1(b). The detailed derivation of the dispersion relation for the fully coupled electromechanical system is presented in Appendix A along with a comparison of the resulting dispersion curves using smooth and square-wave modulation profiles. The experimental setup and the individual setup components are shown in Fig. 2. In the experiments, we consider a clamped-free piezoelectric metamaterial beam with 31 separately bonded pairs of piezoelectric patches. The last piezoelectric pair (at the free end) is reserved for actuation, leaving 30 piezoelectric pairs (i.e., 30 unit cells) that are connected to a synthetic impedance system based on a fully programmable gate array (FPGA) with 32 individually addressable shunt circuits operating at 400 kHz. The impedance of each unit cell is determined by a digital filter $F(z)$, which is connected to a Howland current pump (see Fig. 2). Nearly smooth time modulation is achieved by rapidly updating the digital filter coefficients for each unit cell. The circuit impedances are entered in LABVIEW as analytical expressions of the unit cell index i and an auxiliary index j which represents each time step of the modulation. The corresponding digital filter coefficients are calculated in LABVIEW using the Tustin continuous-to-discrete transformation. To achieve a sufficiently fast update rate (i.e., much faster than the modulation frequency), the full array of coefficients is transferred to memory on the FPGA, such that the coefficients only need to be calculated once per modulation profile. On the FPGA, the digital filter runs continuously, and the filter coefficients are determined by an internal counter that tracks the time step of modulation. The counter is updated by a digital trigger and external pulse train, such that the update rate for the stored impedances (and hence the modulation frequency) can be varied by a waveform generator. The smoothness of the resulting modulation is limited by the number of time steps that can be stored in memory on the FPGA, which in turn depends on the digital filter order and the required numerical precision (e.g., the smallest change in coefficients for each time step). Vibration measurements in terms of the out-of-plane velocity of 300 points along the beam are taken using a Polytec PSV-500 scanning laser Doppler vibrometer (SLDV). The lattice constant of the system is $a = 10.25$ mm, and each unit cell is numbered with index r. The space and time modulation of the piezoelectric metamaterial is performed on the electrical inductance, or equivalently the resonant frequency, associated with each unit cell to generate a pump wave traveling in the positive or negative x directions according to

$$f_r = f_0\left[1 + \alpha_m \sin\left(2\pi f_m t - \frac{2\pi}{3} r\right)\right], \quad r = 1, 2, \ldots, 30, \tag{1}$$

where f_0 is a mean resonant frequency around which modulation takes place, α_m is the modulation amplitude, f_m is the modulation frequency, and r is an index denoting the unit cell number. The system is excited by sending a voltage signal of wideband tone burst to the amplifier connected to the last piezoelectric pair at the free end of the beam. Spatial and temporal Fourier transforms are performed on the

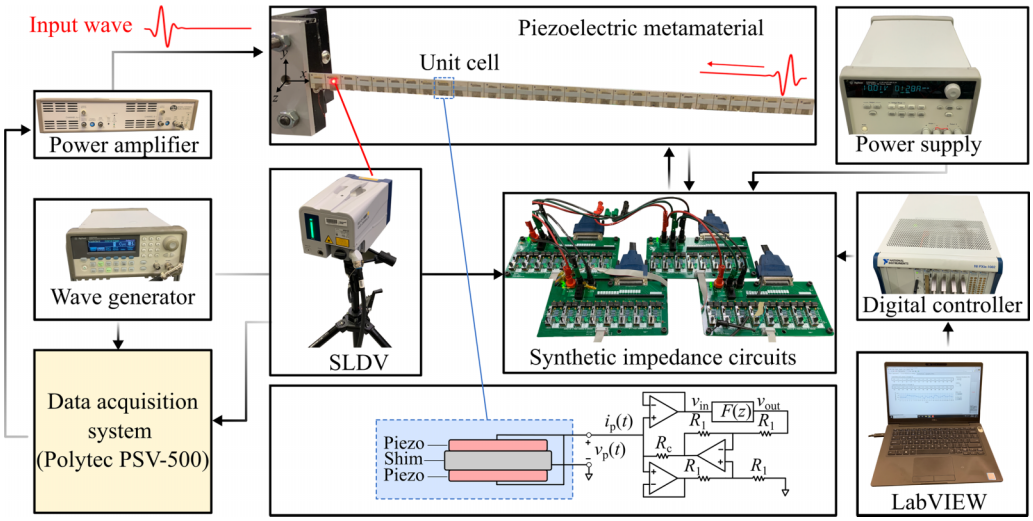

FIG. 2. Illustration of the programmable piezoelectric metamaterial beam and setup components along with a schematic of one unit cell showing a parallel connection of the piezoelectric pair and shunted to a synthetic impedance circuit. The desired circuit impedance values are computed using a LABVIEW script and stored in the digital controller. The power supply is connected to four printed circuit boards, emulating the synthetic impedance circuits. The waveform generator sends a train pulse to switch between impedance values and is synchronized with the measurements taken by the SLDV.

measured out-of-plane velocity field to extract the frequency contents of propagating waves. Note that since excitation occurs at the right end of the waveguide, positive f_m represents a modulation wave traveling in the opposite direction to the excitation while negative f_m represents a modulation wave traveling in the same direction. In order to guide and support the experiments and for a detailed understanding, we use the commercial finite-element software COMSOL MULTIPHYSICS 5.5 (see more details in Appendix B).

B. Dispersion curves and programmable reciprocity breaking

To investigate the nonreciprocal propagation of elastic waves, the experimental setup is tested for the case when the mean resonant frequency is $f_0 = 7500$ Hz, and each experimental run is carried out for positive and negative modulation frequency f_m to reveal the nonreciprocal behavior. Figures 3–5 show the normalized dispersion contours and average frequency spectrum of all points along the piezoelectric metamaterial. In order to clearly compare the experimental results against the numerical simulations, the experimental results are plotted in Figs. 3(a), 4(a), and 5(a), and the numerical simulation results are plotted in Figs. 3(b), 4(b), and 5(b). The modulation frequency f_m is first selected as 0 Hz with modulation amplitude α_m of 0.1 as shown in Fig. 3. At zero modulation frequency, we have spatial modulation only, and the resulting dispersion curves are symmetric with multiple band gaps corresponding to the resonant frequencies of the supercell. Figure 3(b) shows the numerical results which agree well with the experimental results. When the modulation frequency increases to $f_m = 750$ Hz as shown in Fig. 4, the resulting positive and negative band gaps do not overlap, and they open at different frequencies. This results in nonreciprocal behavior in the corresponding dispersion contours. That is, this modulation frequency is sufficient to break the symmetric dispersion curves of Fig. 3 at the same modulation amplitude. Since nonreciprocal wave propagation is proved to exist for $f_m = 750$ Hz, we next increase the modulation amplitude to $\alpha_m = 0.15$ as shown in Fig. 5. At this modulation amplitude, the positive and negative band gaps separate farther from each other. The positive band gap opens around 8000 Hz for the experimental and numerical results. The negative band gap opens around 7000 Hz. Interestingly, we also observe the opening of an additional negative band gap around 9000 Hz. It is evident from these findings that increasing the modulation amplitude results in strong nonreciprocity as the separation between the positive and negative band gaps becomes larger. Particularly, the negative band gaps shrink in size and shift to lower frequencies. Note that in these results, reciprocity breaking takes place near the resonant frequencies of the unit cells, an advantage over, for example, modulating the capacitance to observe nonreciprocity near Bragg band gaps. Additionally, the inductive modulation considered here would still open nonreciprocal Bragg band gaps due to the impedance mismatch in the unit cells, something not captured in the experimental and numerical results due to the finite size of the system and the limited number of available unit cells. (This is shown later in Fig. 11 under the assumption of infinite piezoelectric metamaterial where directional Bragg band gaps are observed in addition to the directional band gaps observed here.) One unique feature of leveraging synthetic impedance circuits is the ease of control of the modulation parameters such that the mean frequency, modulation frequency, and amplitude can be modified in the LABVIEW interface. Figure 6 shows the dispersion contours corresponding to the case when the mean frequency $f_0 = 4000$ Hz, modulation amplitude $\alpha_m = 0.2$, and modulation frequency $f_m = 400$ Hz. As expected, the dispersion curves are nonreciprocal, showing negative and positive band gaps that open at different frequencies. Note that since the modulation amplitude α_m is large, multiple band gaps are clearly shown in the dispersion curves.

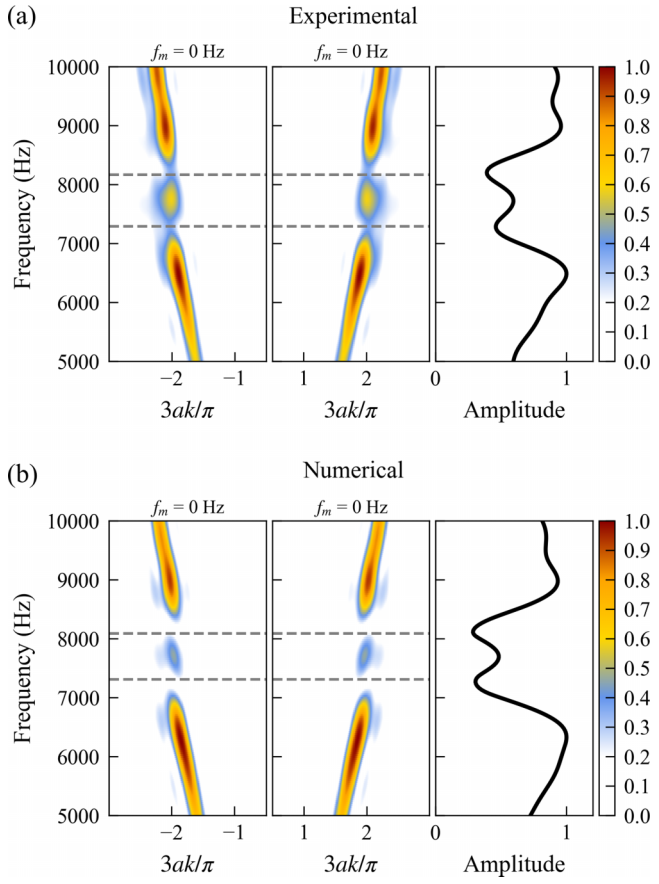

FIG. 3. Results [two-dimensional (2D) fast Fourier transform (FFT) to extract space-time behavior] for $f_0 = 7500$ Hz, $f_m = 0$ Hz, and $\alpha_m = 0.1$. (a) Experimental results. (b) Numerical simulations. Here, the dashed gray lines indicate the mean frequency of band gaps.

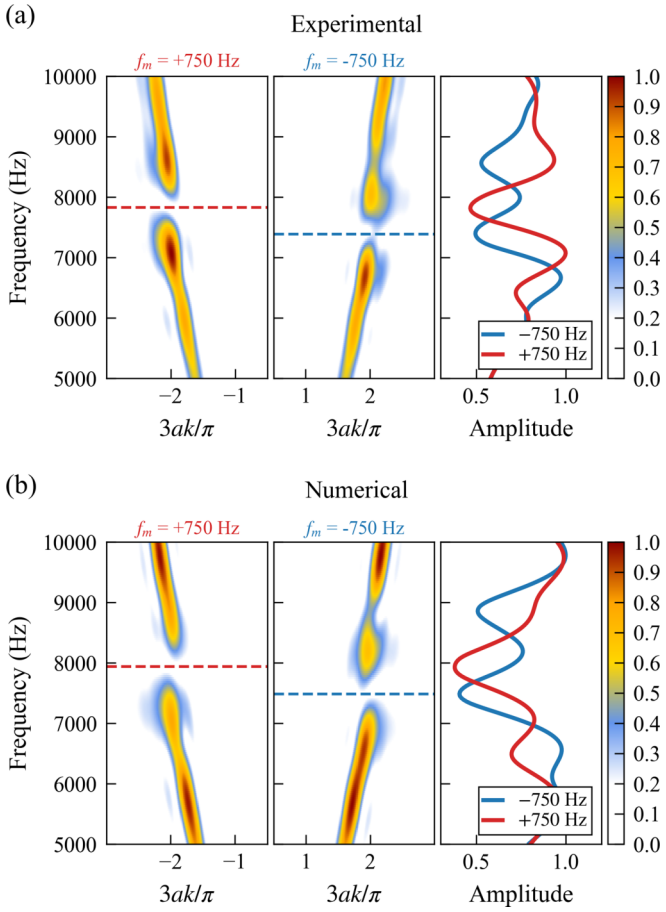

FIG. 4. Results (2D FFT to extract space-time behavior) for $f_0 = 7500$ Hz, $f_m = 750$ Hz, and $\alpha_m = 0.1$. (a) Experimental results. (b) Numerical simulations. The resulting frequency band gaps under positive and negative modulation are separated and do not overlap, indicating nonreciprocal wave propagation. Here, the dashed blue lines indicate the mean frequency of band gaps under negative modulation, while the dashed red lines indicate the mean frequency of band gaps under positive modulation.

C. Narrow-band excitation and frequency conversion

The experimental and numerical findings discussed above highlight the negative and positive frequency band gaps for different levels of modulation frequency and amplitude. We aim to have more understanding of what would happen for propagating waves with a central frequency that lies within one of the highlighted band gaps. For this purpose, we examine the case when the modulation parameters are $f_m = 750$ Hz and $\alpha_m = 0.15$ (same modulation parameters used in Fig. 5) but this time by sending a narrow-band excitation with a central frequency of $f_c = 8000$ Hz. We then examine the frequency spectrum of spatial points within 15 and 85% of the beam length, after the clamped end and before the actuation piezo near the beam's tip. The goal here is to see the frequency spectrum of the propagating waves away from the dominant frequency spectrum at the excitation position, the last unit cell at $x/L = 1$. The frequency spectrum is shown in Fig. 7 for positive and negative modulation frequencies. For negative modulation, $f_m = -750$ Hz, the waves propagate through the metamaterial beam as indicated by the high amplitude at the central frequency shown by the black horizontal dashed line in Figs. 7(a) and 7(c). On the other hand, when the modulation frequency is positive, $f_m = 750$ Hz, wave attenuation is observed through the metamaterial beam at the central frequency. In addition, for both positive and negative modulations, we observe propagating waves with central frequencies above and below the center frequency of the excitation (shown by magenta dashed lines). This is an indication of the frequency conversion of the incident waves from the excitation source. This frequency conversion is related to the modulation frequency f_m as it is centered at $f_c \pm f_m$. Figures 7(b) and 7(d) show the frequency spectrum at the center of the beam under positive and negative modulations compared with that under no modulation (i.e., $f_m = 0$ Hz), along with the excitation spectrum. The frequency spectrum in each case is normalized with respect to the highest amplitude among the three cases. Again, the amplitude of the propagating waves under positive modulation at f_c is smaller than that under negative modulation but higher at $f_c \pm f_m$. Moreover, the unmodulated case ($f_m = 0$ Hz) does not show any frequency conversion of the excited waves with the highest amplitude at the central frequency f_c. Note that the differences in the average frequency spectrum between the positive modulation in the numerical

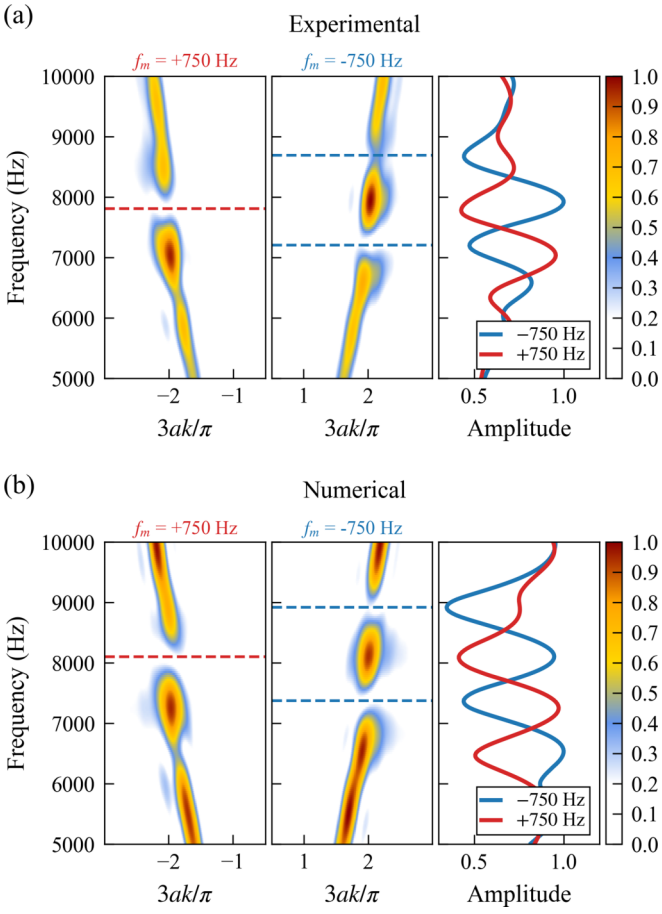

FIG. 5. Results (2D FFT to extract space-time behavior) for $f_0 = 7500$ Hz, $f_m = 750$ Hz, and $\alpha_m = 0.15$. (a) Experimental results. (b) Numerical simulations. At this increased modulation amplitude, the positive and negative band gaps shift even farther. Here, the dashed blue lines indicate the mean frequency of band gaps under negative modulation, while the dashed red lines indicate the mean frequency of band gaps under positive modulation.

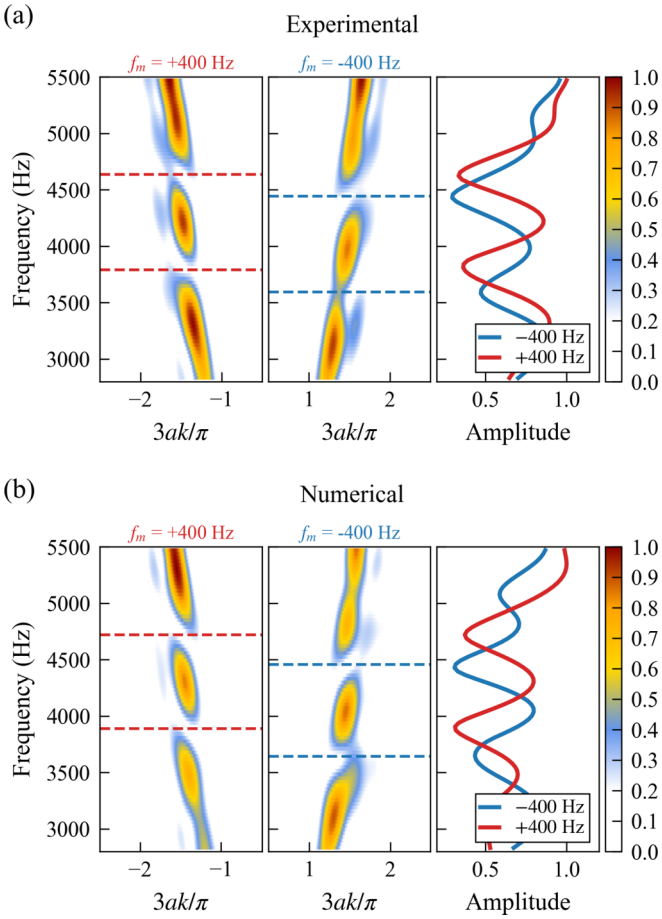

FIG. 6. Results (2D FFT to extract space-time behavior) for $f_0 = 4000$ Hz, $f_m = 400$ Hz, and $\alpha_m = 0.2$. (a) Experimental results. (b) Numerical simulations. Here, the dashed blue lines indicate the mean frequency of band gaps under negative modulation, while the dashed red lines indicate the mean frequency of band gaps under positive modulation.

and experimental results are expected to be a result of the mismatch between the experimental and numerical band-gap frequencies [cf. Figs. 5(a) and 5(b) for positive modulation band gaps]. However, this mismatch is not pronounced in the case of negative modulation, as the 8000 Hz frequency lies within the propagation band for negative modulation. The emergence of waves with central frequencies shifted by $\pm f_m$ with respect to f_c is explained as a Doppler-like effect [44]. The positive modulation of the resonant frequencies induces a pump wave traveling in the opposite direction to the exciting waves; as a result, the waves decay faster at f_c and are reflected at frequencies $f_c \pm f_m$. This is clearly shown in Figs. 7(a) and 7(c), in which the amplitudes of the reflected waves are prominent over a distance close to the excitation end (from $x/L = 0.5$ to $x/L = 0.85$). To further illustrate this, we increase the modulation frequency to $f_m = 900$ Hz (see Fig. 8). The resulting frequency spectrum confirms the frequency conversion of waves, only this time the reflected waves under positive modulation have central frequencies that are shifted farther from the f_c as the modulation frequency, in this case, is $f_m = 900$ Hz. Note that in both Figs. 7 and 8 there is significant attenuation both at the center frequency f_c and the shifted frequencies $f_c \pm f_m$. There are numerous sources of damping in the experimental system, most notably the thin layer of epoxy between the piezoelectric patches and the underlying aluminum structure (see Appendix B). Although a vacuum-bonding process was used to minimize the thickness of this epoxy layer, it introduces significant attenuation, especially near the local resonance frequency, where the curvature of the piezoelectric patches is highest. Additionally, the synthetic impedance system allows variation of the damping in the electrical circuit: Here, we apply identical electrical damping to each unit cell such that the overall system is stable, but further minimization on a cell-by-cell basis would further minimize the attenuation in the system.

Figure 9 illustrates the average numerical frequency spectra at $x/L = 0.5$, covering both positive and negative modulation frequencies within the range 600–1000 Hz. The figure highlights the negligible frequency conversion observed at low modulation frequencies, as indicated by the dashed magenta lines representing the amplitude at $f_c \pm f_m$ for each case. The absence of significant frequency conversion can be attributed to the central frequency lying outside the directional

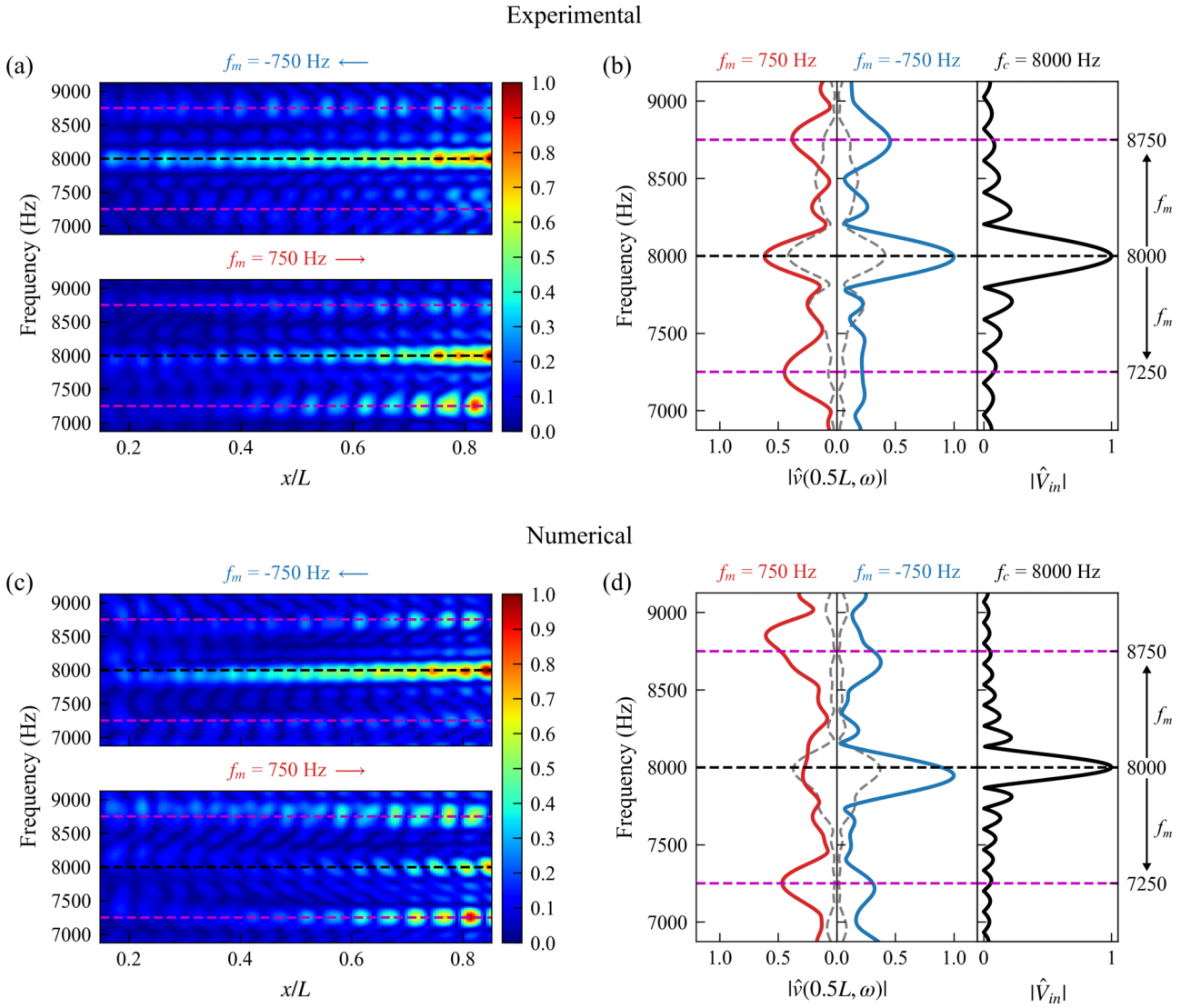

FIG. 7. Results for $f_0 = 7500$ Hz, $f_m = 750$ Hz, and $\alpha_m = 0.15$ under a narrow-band excitation centered at $f_c = 8000$ Hz. Experimental (a) and numerical (c) frequency spectra within 15–85% of the beam length. The horizontal black and magenta lines denote f_c and $f_c \pm f_m$, respectively. Experimental (b) and numerical (d) average frequency spectra of three points at $x/L = 0.5$. The thin dashed gray response corresponds to the case $f_m = 0$.

band gaps. As previously demonstrated, the directional band gaps occur around a modulation frequency of approximately 750 Hz in this particular scenario.

III. DISCUSSION

We have developed a resonant, nonreciprocal, and fully programmable piezoelectric metamaterial waveguide using unit cells shunted to inductive synthetic impedance circuits digitally controlled for modulation in space and time. The experimental setup offers smooth spatiotemporal modulation of the properties of the metamaterial unit cells (without requiring analog switches) as well as the precise selection of the relevant spatiotemporal modulation parameters, allowing for digitally programmable reciprocity breaking. In addition, through locally resonant modulation, nonreciprocity is observed independent of the Bragg band-gap location. The experimental and numerical results show the effects of spatiotemporal modulation in terms of directional band gaps in the dispersion contours. The directional band gaps were observed for different modulation parameters such as mean resonant frequency, modulation amplitude, and modulation frequency. The results suggest that increasing the modulation amplitude results in strong nonreciprocity breaking. Also, when a narrow-band excitation is centered at one of the directional band gaps, we observe propagating waves with central frequencies shifted by approximately the modulation frequency value. This class of synthetic-impedance-based programmable piezoelectric metamaterials offers a platform that allows for the exploration of many concepts concerned with time and/or space modulation of unit cells' properties to achieve, for example, frequency conversion, topological pumping, parity-time symmetry, and roton-like dispersion [45,46].

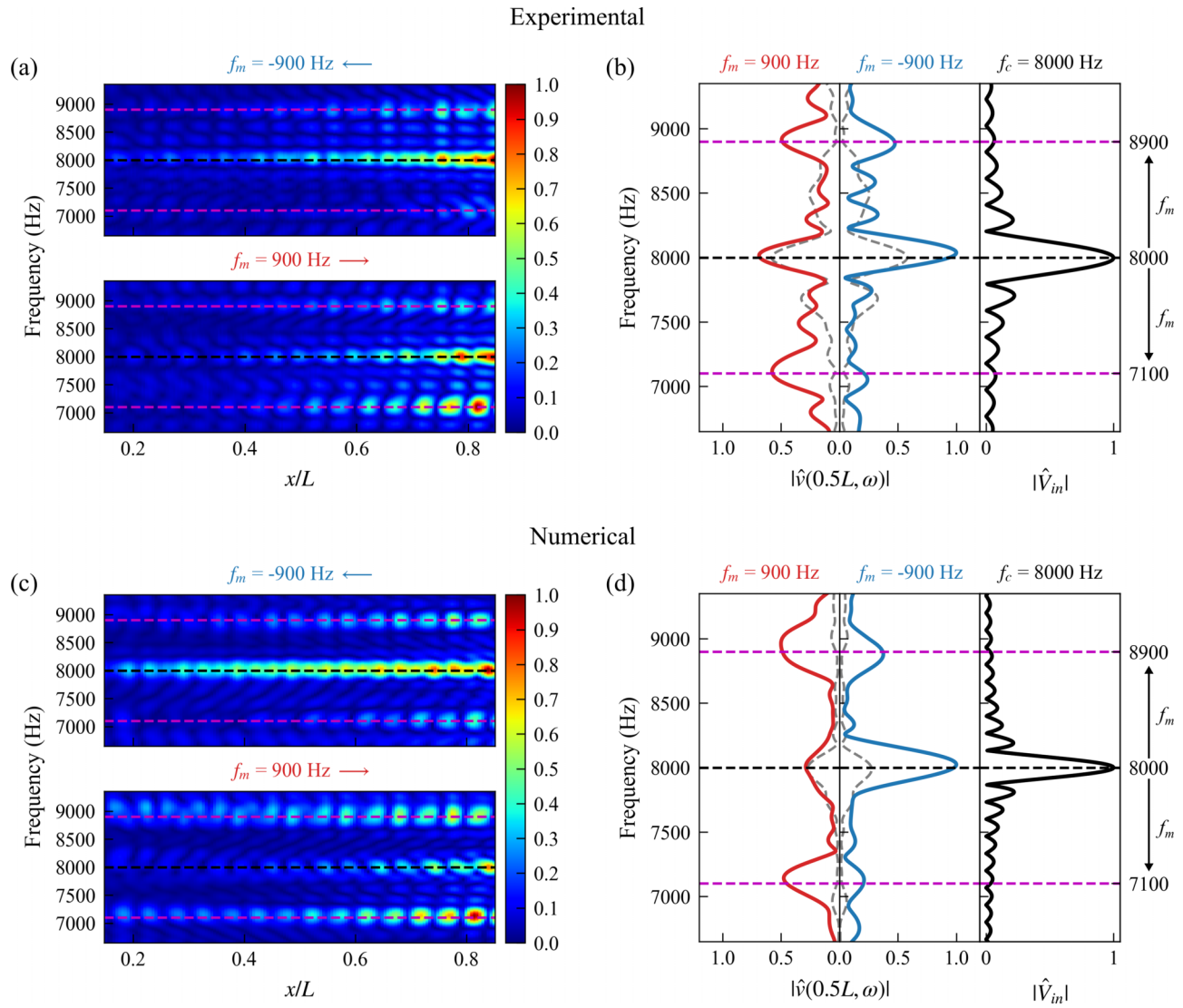

FIG. 8. Results for $f_0 = 7500$ Hz, $f_m = 900$ Hz, and $\alpha_m = 0.15$ under a narrow-band excitation centered at $f_c = 8000$ Hz. Experimental (a) and numerical (c) frequency spectra within 15–85% of the beam length. The horizontal black and magenta lines denote f_c and $f_c \pm f_m$, respectively. Experimental (b) and numerical (d) average frequency spectra of three points at $x/L = 0.5$. The thin dashed gray response corresponds to the case $f_m = 0$.

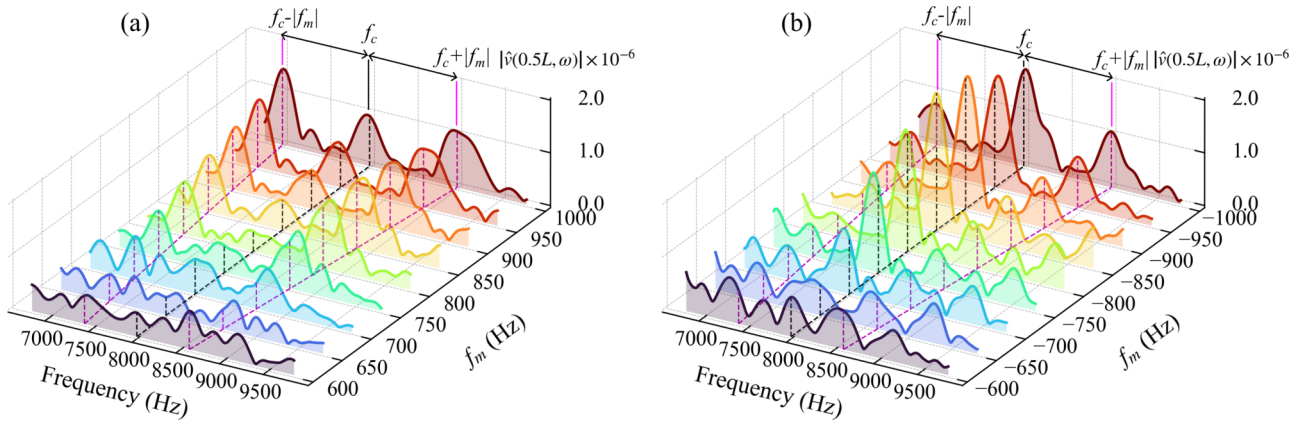

FIG. 9. Numerical average frequency spectra of three points at $x/L = 0.5$ under a narrow-band excitation centered at $f_c = 8000$ Hz, with $f_0 = 7500$ Hz and $\alpha_m = 0.15$. The spectra are shown for two ranges of modulation frequencies: (a) 600–1000 Hz and (b) −600 to −1000 Hz. These spectra provide insights into the frequency conversion phenomenon resulting from the interaction between the narrow-band excitation and the system.

ACKNOWLEDGMENT

Support from the Woodruff Professorship and Carl Ring Family Chair endowments (held by Prof. Alper Erturk at Georgia Tech) is acknowledged.

APPENDIX A: DISPERSION CURVES OF THE ELECTROMECHANICAL UNIT CELLS

Consider an infinite piezoelectric Euler-Bernoulli beam composed of repeated piezoelectric layers bonded on the top and bottom surfaces of the beam shown in Fig. 10. Pairs of segmented electrode layers, of negligible thickness, cover the top and the bottom surfaces of the top and bottom piezoelectric layers, respectively. The electrode pairs are separated by a distance of $2a$. The governing electromechanical equations describing the transverse displacement of the beam $w(x,t)$ and the output voltage $v_{rq}(t)$ across the qth electrode pair are

$$\mathrm{EI}\frac{\partial^4 w(x,t)}{\partial x^4} + m\frac{\partial^2 w(x,t)}{\partial t^2} - \theta \sum_{q=0}^{Q-1}\sum_{r=-\infty}^{\infty} v_{rq}(t) \times \frac{d^2}{dx^2}\left[H\left(x - x_{rq}^L\right) - H\left(x - x_{rq}^R\right)\right] = 0 \tag{A1}$$

and

$$C_{p,rq}\frac{\partial v_{rq}(t)}{\partial t} + \theta \int_{x_{rq}^L}^{x_{rq}^R} \frac{\partial^3 w(x,t)}{\partial x^2 \partial t} dx = -i_{rq}(t), \tag{A2}$$

where r goes from $-\infty$ to ∞, $H(x)$ is the Heaviside function, and x_{rq}^L and x_{rq}^R are the coordinates of the left-hand-side edge and the right-hand-side edge of the qth electrode pair in the r array given as

$$x_{rq}^L = r\lambda_m + qL + a, \tag{A3}$$

$$x_{rq}^R = r\lambda_m + (q+1)L - a, \tag{A4}$$

where the spatial period $\lambda_m = QL$ defines the supercell's size. The short-circuit flexural rigidity of the structure (substructure + piezoelectric layers) is

$$\mathrm{EI} = \frac{2b}{3}\left(c_s\frac{h_s^3}{8} + \bar{c}_{11}^E\left[\left(h_p + \frac{h_s}{2}\right)^3 - \frac{h_s^3}{8}\right]\right), \tag{A5}$$

and the equivalent mass per unit length is

$$m = b(\rho_s h_s + 2\rho_p h_p), \tag{A6}$$

where b is the beam's width (also the piezoelectric layers' width), c_s is the substructure's (beam's) elastic modulus, h_s is the substructure's thickness, $\bar{c}_{11}^E$ is the piezoelectric layers' elastic modulus at constant electric field, and h_p is the piezoelectric layers' thickness. The electromechanical coupling coefficient is

$$\theta = \frac{\bar{e}_{31} b_e}{h_p}\left[\left(h_p + \frac{h_s}{2}\right)^2 - \frac{h_s^2}{4}\right], \tag{A7}$$

and the inherent piezoelectric capacitance across the nth electrode pair is

$$C_{p,qr} = \bar{\varepsilon}_{33}^S b_e \frac{x_{qr}^R - x_{qr}^L}{2h_p}, \tag{A8}$$

where $\bar{e}_{31}$ is the effective piezoelectric stress constant, b_e is the electrode's width (for convenience, we assume it is equal to b and omit the subscript "e" in the following equations), and $\bar{\varepsilon}_{33}^S$ is the permittivity component at constant strain. Note that the difference $x_{qr}^R - x_{qr}^L$ defines the electrode's length, which is constant in our case because we assumed geometrically identical unit cells. In other words, the inherent piezoelectric capacitance is identical in all unit cells; therefore the subscripts q and r can be dropped, leading to

$$C_p = \bar{\varepsilon}_{33}^S b \frac{l}{2h_p}, \tag{A9}$$

where, again, l is the electrode layer's length. Assume that the voltage across unit cells changes periodically in time

$$v_{rq}(t) = e^{i\omega t}\sum_{l=-\infty}^{+\infty} V_{rql} e^{il\omega_m t}. \tag{A10}$$

Likewise, assume plane-wave solutions for the transverse displacement of the beam $w(x,t)$ of the form

$$w(x,t) = e^{i(\omega t - \mathbf{k}x)}\sum_{n=-\infty}^{+\infty}\sum_{l=-\infty}^{+\infty} W_{nl} e^{i(l\omega_m t - nk_m x)}, \tag{A11}$$

where $k_m = \frac{2\pi}{\lambda_m}$ is the reciprocal lattice vector, $\mathbf{k}$ is the Bloch wave vector, and W_{nl} is the plane-wave amplitude. Substituting Eqs. (A10) and (A11) into the transverse displacement and voltage equations and dropping the common exponent $e^{i(\omega + l\omega_m)t}$ yield

$$\sum_{n=-\infty}^{+\infty}\sum_{l=-\infty}^{+\infty}\left[\mathrm{EI}(\mathbf{k} + nk_m)^4 - m\omega^2 - 2ml\omega_m\omega - ml^2\omega_m^2\right] \times W_{nl} e^{-i(\mathbf{k}+nk_m)x} - \theta\sum_{l=-\infty}^{+\infty}\sum_{q=0}^{Q-1}\sum_{r=-\infty}^{+\infty} V_{rql} \times \frac{d^2}{dx^2}\left[H\left(x - x_{rq}^L\right) - H\left(x - x_{rq}^R\right)\right] = 0 \tag{A12}$$

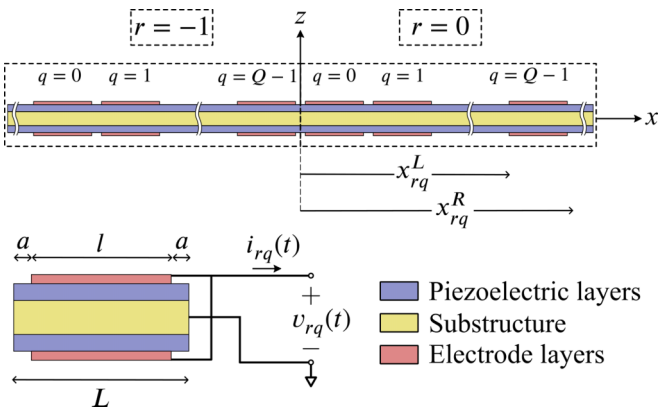

FIG. 10. Schematic of an undamped infinite bimorph piezoelectric beam covered by segmented electrodes. The primitive unit cell consists of a single pair of electrodes, two piezoelectric layers, and the central shim (substructure). A group of Q primitive unit cells forms the repeated supercell of the system.

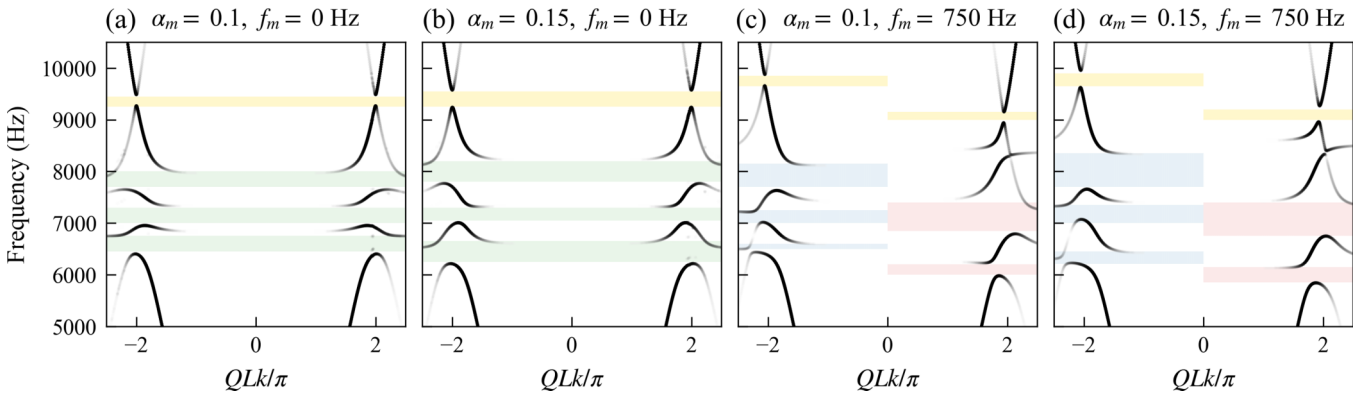

FIG. 11. Dispersion curves for (a) and (b) space-only and (c) and (d) space-time modulated piezoelectric waveguides. Shaded yellow regions represent Bragg band gaps, while shaded red, blue, and green regions represent locally resonant band gaps.

and

$$\sum_{l=-\infty}^{+\infty} iC_p(\omega + l\omega_m)V_{rql}e^{il\omega_m t} - i\theta \sum_{n=-\infty}^{+\infty}\sum_{l=-\infty}^{+\infty} e^{il\omega_m t} \times (\mathbf{k}+nk_m)^2(\omega + l\omega_m)W_{nl}\int_{x_{rq}^L}^{x_{rq}^R} e^{-i(\mathbf{k}+nk_m)x}dx = -e^{-i\omega t}i_{rq}(t). \tag{A13}$$

Note that we can simplify the integral in the above equation by realizing that the system is periodic, meaning the integral over the qth unit cell in the rth supercell is equivalent to that in the 0th supercell. Thus we can shift the spatial coordinates in the exponential by $r\lambda_m$. That is,

$$\int_{x_{0q}^L}^{x_{0q}^R} e^{-i(\mathbf{k}+nk_m)(x-r\lambda_m)}dx = e^{-ir\lambda_m}\int_{x_{0q}^L}^{x_{0q}^R} e^{-i(\mathbf{k}+nk_m)x}dx. \tag{A14}$$

Evaluating the integral

$$\int_{x_{0rl}^L}^{x_{0rl}^R} e^{-i(\mathbf{k}+nk_m)x}dx = \frac{i}{(\mathbf{k}+nk_m)}e^{-iLq(\mathbf{k}+nk_m)} \times \left[e^{-iL(\mathbf{k}+nk_m)}e^{ia(\mathbf{k}+nk_m)} - e^{-ia(\mathbf{k}+nk_m)}\right] \tag{A15}$$

and substituting the result into Eq. (A13),

$$\sum_{l=-\infty}^{+\infty} iC_p(\omega + l\omega_m)V_{rql}e^{il\omega_m t} + \theta e^{-ir\lambda_m}\sum_{n=-\infty}^{+\infty}\sum_{l=-\infty}^{+\infty} e^{il\omega_m t}(\mathbf{k}+nk_m)(\omega + l\omega_m)W_{nl} \times e^{-iLq(\mathbf{k}+nk_m)}\left[e^{-iL(\mathbf{k}+nk_m)}e^{ia(\mathbf{k}+nk_m)} - e^{-ia(\mathbf{k}+nk_m)}\right] = -e^{-i\omega t}i_{rq}(t). \tag{A16}$$

This implies

$$V_{rql} = V_{0ql}e^{-ir\lambda_m}, \tag{A17}$$

which means it is sufficient to know the voltage across the qth unit cell to compute all voltages across the qth unit cell in the rth supercell. Multiply by $e^{ir\lambda_m}$:

$$\sum_{l=-\infty}^{+\infty} iC_p(\omega + l\omega_m)V_{0ql}e^{il\omega_m t} + \theta \sum_{n=-\infty}^{+\infty}\sum_{l=-\infty}^{+\infty} e^{il\omega_m t} \times (\mathbf{k}+nk_m)(\omega + l\omega_m)W_{nl}e^{-iLq(\mathbf{k}+nk_m)} \times \left[e^{-iL(\mathbf{k}+nk_m)}e^{ia(\mathbf{k}+nk_m)} - e^{-ia(\mathbf{k}+nk_m)}\right] = e^{ir\lambda_m}e^{-i\omega t}i_{rq}(t) \tag{A18}$$

or

$$\sum_{l=-\infty}^{+\infty} iC_p(\omega + l\omega_m)V_{0ql}e^{il\omega_m t} + \theta \sum_{n=-\infty}^{+\infty}\sum_{l=-\infty}^{+\infty} e^{il\omega_m t} \times (\omega + l\omega_m)W_{nl}\mathcal{D}(n) = -e^{ir\lambda_m}e^{-i\omega t}i_{rq}(t), \tag{A19}$$

where

$$\mathcal{D}(n) = (\mathbf{k}+nk_m)e^{-iLq(\mathbf{k}+nk_m)} \times \left[e^{-iL(\mathbf{k}+nk_m)}e^{ia(\mathbf{k}+nk_m)} - e^{-ia(\mathbf{k}+nk_m)}\right]. \tag{A20}$$

The input current i_{0ql} in Eq. (A13) will be evaluated once the circuit components are determined. Multiply Eq. (A12) by $e^{i\mathbf{k}x}$:

$$\sum_{n=-\infty}^{+\infty}\sum_{l=-\infty}^{+\infty}\left[\mathrm{EI}(\mathbf{k}+nk_m)^4 - m\omega^2 - 2ml\omega_m\omega - ml^2\omega_m^2\right] \times W_{nl}e^{-ink_m x} + \theta\sum_{l=-\infty}^{+\infty}\sum_{q=0}^{Q-1}V_{0ql}\sum_{r=-\infty}^{+\infty}e^{i(\mathbf{k}x-r\lambda_m)} \times \frac{d^2}{dx^2}\left[H\left(x-x_{rq}^L\right) - H\left(x-x_{rq}^R\right)\right] = 0. \tag{A21}$$

The summation over r produces a periodic function in space with periodicity λ_m that can be expanded in a Fourier series. That is,

$$\sum_{r=-\infty}^{+\infty} e^{i(\mathbf{k}x-r\lambda_m)}\frac{d^2}{dx^2}\left[H\left(x-x_{rq}^L\right) - H\left(x-x_{rq}^R\right)\right] = \frac{i}{\lambda_m}\sum_{n=-\infty}^{\infty}\mathcal{D}^*(n)e^{-ink_m x}, \tag{A22}$$

where $(\,)^*$ denotes the complex conjugate. Substituting Eq. (A22) into Eq. (A21),

$$\sum_{n=-\infty}^{+\infty}\sum_{l=-\infty}^{+\infty}\left[\mathrm{EI}(\mathbf{k}+nk_m)^4-m\omega^2-2ml\omega_m\omega-ml^2\omega_m^2\right]\times W_{nl}e^{-ink_mx}-\frac{i\theta}{\lambda_m}\sum_{l=-\infty}^{+\infty}\sum_{q=0}^{Q-1}V_{0ql}\sum_{n=-\infty}^{+\infty}\mathcal{D}^*(n)e^{-ink_mx}=0. \tag{A23}$$

Dropping the common exponent e^{-ink_mx} yields

$$\sum_{n=-\infty}^{+\infty}\sum_{l=-\infty}^{+\infty}\left[\mathrm{EI}(\mathbf{k}+nk_m)^4-m\omega^2-2l\omega_m\omega-l^2\omega_m^2\right]\times W_{nl}-\frac{i\theta}{\lambda_m}\sum_{l=-\infty}^{+\infty}\sum_{q=0}^{Q-1}V_{0ql}\sum_{n=-\infty}^{+\infty}\mathcal{D}^*(n)=0. \tag{A24}$$

The input current $i_{rq}(t)$ in Eq. (A19) depends on the external circuit. If inductive circuits are used, then the input current is

$$i_{rq}(t)=\int_t L_q^{-1}(t)v_{rq}(t)dt, \tag{A25}$$

where $L_q(t)$ is the time modulated inductance in the external circuit connected to the qth unit cell. Assuming that the reciprocal of the inductance is changing periodically in time with a modulation frequency of ω_m, it can be expanded with a Fourier series of the form

$$L_q^{-1}(t)=\sum_{p=-\infty}^{\infty}\hat{L}_{qp}^{-1}e^{ip\omega_mt}, \tag{A26}$$

where

$$\hat{L}_{qp}^{-1}=\frac{1}{T_m}\int_{-T_m/2}^{T_m/2}L_q^{-1}(t)e^{-ip\omega_mt}dt \tag{A27}$$

are the Fourier coefficients. Recall that the voltage is given as

$$v_{rq}(t)=e^{i\omega t}\sum_{l=-\infty}^{+\infty}V_{rql}e^{il\omega_mt}. \tag{A28}$$

Thus

$$i_{rq}(t)=\sum_{p=-\infty}^{\infty}\sum_{l=-\infty}^{\infty}\frac{1}{i[(l+p)\omega_m+\omega]}\hat{L}_{qp}^{-1}V_{rql}e^{it[(l+p)\omega_m+\omega]}, \tag{A29}$$

and Eq. (A19) becomes

$$\sum_{l=-\infty}^{+\infty}iC_p(\omega+l\omega_m)V_{0ql}e^{il\omega_mt}+\theta\sum_{n=-\infty}^{+\infty}\sum_{l=-\infty}^{+\infty}e^{il\omega_mt}(\omega+l\omega_m)W_{nl}\mathcal{D}(n)=-e^{ir\lambda_m}e^{-i\omega t}\sum_{p=-\infty}^{\infty}\sum_{l=-\infty}^{\infty}\frac{1}{i[(l+p)\omega_m+\omega]}\times\hat{L}_{qp}^{-1}V_{rql}e^{it[(l+p)\omega_m+\omega]}. \tag{A30}$$

Simplify:

$$\sum_{l=-\infty}^{+\infty}iC_p(\omega+l\omega_m)V_{0ql}e^{il\omega_mt}+\theta\sum_{n=-\infty}^{+\infty}\sum_{l=-\infty}^{+\infty}e^{il\omega_mt}(\omega+l\omega_m)W_{nl}\mathcal{D}(n)=-\sum_{p=-\infty}^{\infty}\sum_{l=-\infty}^{\infty}\frac{1}{i[(l+p)\omega_m+\omega]}\hat{L}_{qp}^{-1}V_{0ql}e^{i(p+l)\omega_mt}. \tag{A31}$$

Exploiting the orthogonality of exponential functions, multiply Eq. (A31) by $(1/T_m)e^{-ih\omega_mt}$, where h is an arbitrary integer, and integrate over time from $-T_m/2$ to $T_m/2$ to obtain

$$iC_p(\omega+h\omega_m)V_{0qh}+\theta\sum_{n=-\infty}^{+\infty}(\omega+h\omega_m)W_{nh}\mathcal{D}(n)=-\sum_{p=-\infty}^{\infty}\frac{1}{i[h\omega_m+\omega]}\hat{L}_{qp}^{-1}V_{0q,h-p}. \tag{A32}$$

Multiply by $(h\omega_m+\omega)$:

$$C_p(\omega+h\omega_m)^2V_{0qh}-i\theta\sum_{n=-\infty}^{+\infty}(\omega+h\omega_m)^2W_{nh}\mathcal{D}(n)=\sum_{p=-\infty}^{\infty}\hat{L}_{qp}^{-1}V_{0q,h-p}. \tag{A33}$$

Since h is arbitrary, switch back to l. In summary, we have

$$\sum_{n=-\infty}^{+\infty}\sum_{l=-\infty}^{+\infty}\left[\mathrm{EI}(\mathbf{k}+nk_m)^4-m\omega^2-2ml\omega_m\omega-ml^2\omega_m^2\right]\times W_{nl}-\frac{i\theta}{\lambda_m}\sum_{l=-\infty}^{+\infty}\sum_{q=0}^{Q-1}V_{0ql}\sum_{n=-\infty}^{+\infty}\mathcal{D}^*(n)=0, \tag{A34}$$

$$C_p(\omega+l\omega_m)^2V_{0ql}-\sum_{p=-\infty}^{\infty}\hat{L}_{qp}^{-1}V_{0q,l-p}-i\theta\sum_{n=-\infty}^{+\infty}(\omega+l\omega_m)^2W_{nl}\mathcal{D}(n)=0. \tag{A35}$$

If the infinite sums in Eqs. (A34) and (A35) are truncated at some finite value, one can solve a quadratic eigenvalue problem (QEP). For a maximum plane-wave index N and maximum harmonic index L the total number of unknown coefficients that can be solved for is

$$N_{\mathrm{tot}}=[(2N+1)+Q](2L+1). \tag{A36}$$

1. Sinusoidal modulation

The resonant frequency of the qth unit cell is assumed to take the form

$$f_q(t)=f_0[1+\alpha_m\sin(2\pi f_mt-Lk_mq)], \tag{A37}$$

where $q = 1, 2, \ldots, Q-1$, $k_m = 2\pi/\lambda_m$, f_m is the modulation frequency, and α_m is the modulation amplitude. Since $(2\pi f_q)^2 = 1/(L_q C_p)$, the sinusoidal modulation in Eq. (A37) can be achieved by modulating the corresponding inductance reciprocal as

$$L_q^{-1}(t) = 4\pi^2 f_0^2 C_p [1 + \alpha_m \sin(2\pi f_m t - L k_m q)]^2. \quad \text{(A38)}$$

With this, the Fourier coefficients in Eq. (A27) are given as

$$\hat{L}_{qp}^{-1} = \begin{cases} -\pi^2 C_p \alpha_m^2 f_0^2 e^{i2Lk_m q} & \text{for } p = -2 \\ i4\pi^2 C_p \alpha_m f_0^2 e^{iLk_m q} & \text{for } p = -1 \\ 2\pi^2 C_p f_0^2 \left(\alpha_m^2 + 2\right) & \text{for } p = 0 \\ -i4\pi^2 C_p \alpha_m f_0^2 e^{-iLk_m q} & \text{for } p = 1 \\ -\pi^2 C_p \alpha_m^2 f_0^2 e^{-i2Lk_m q} & \text{for } p = 2 \\ 0 & \text{otherwise.} \end{cases} \quad \text{(A39)}$$

The dispersion curve for the case when the modulation frequency $f_m = 0$ and modulation amplitude $\alpha_m = 0.1$ is shown in Fig. 11(a). As expected, in the absence of the modulation frequency, the dispersion curve is symmetric with multiple band gaps corresponding to the resonant frequencies of the three primitive unit cells and the well-known Bragg band gap occurring at the points $QkL/\pi = \pm 2$ due to the variation of the impedance within the supercell. When the modulation amplitude increases to $\alpha_m = 0.15$, the impedance mismatch increases, and the Bragg band gap becomes wider [see Fig. 11(b)]. For $\alpha_m = 0.1$ and $f_m = 750$ Hz shown in Fig. 11(c), the dispersion curve is no longer symmetric, and we observe multiple nonreciprocal band gaps. The left Bragg band gap shifts to a higher frequency, while the right one shifts to a lower frequency. In addition, the highest left-hand-side resonant band gap becomes wider, while the right-hand-side resonant band gap closes, resulting in nonreciprocal wave propagation at 8000 Hz (waves propagate in the right direction only). Increasing the modulation amplitude to $\alpha_m = 0.15$ results in wider band gaps as shown in Fig. 11(d). Note that due to the finite size of the experimental piezoelectric metamaterials and the limited number of unit cells (31 unit cells), the Bragg band gaps shown here do not appear in the dispersion curves of Figs. 3–5.

2. Square-wave modulation

Instead of the sinusoidal modulation profile given by Eq. (A37), consider the following square-wave modulation:

$$f_q(t) = f_0(1 - \alpha_m) + 2 f_0 \alpha_m H[\sin(2\pi f_m t - L k_m q)], \quad \text{(A40)}$$

with the Fourier coefficients given by

$$\hat{L}_{qp}^{-1} = 4\pi^2 C_p f_0^2 \left(\alpha_m^2 + 1\right) \quad \text{for } p = 0 \quad \text{(A41)}$$

and

$$\hat{L}_{qp}^{-1} = -\frac{i8\pi}{p} C_p \alpha_m f_0^2 ((-1)^p - 1) e^{-ip(Lk_m q + \pi)} \quad \text{(A42)}$$

otherwise. Figure 12 shows a comparison of the resulting dispersion curves using sinusoidal and square-wave modulation profiles with a maximum harmonic index of $L = 10$, a modulation amplitude of $\alpha_m = 0.15$, and a modulation frequency of $f_m = 750$ Hz. The dispersion curves of the square-wave modulation case are more polluted due to the large number of harmonics compared with the sinusoidal case.

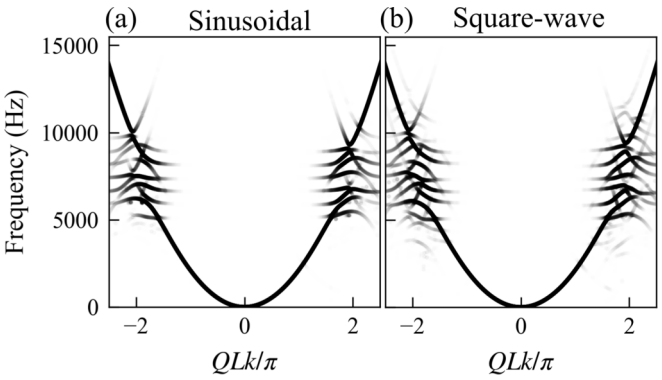

FIG. 12. Dispersion curves for (a) sinusoidal and (b) square-wave modulation profiles. In (b), more dispersion branches are apparent due to the larger number of harmonics.

APPENDIX B: METHODS

1. Fabrication and design of the experiment

The programmable piezoelectric metamaterial is made of a conductive shim (aluminum 6061) with dimensions 307×10×0.75 mm hosting square piezoelectric patches [lead zirconate titanate (PZT-5A)], each with dimensions of 10×10×0.3 mm. The piezoelectric patches are vacuum bonded to the conductive shim with epoxy (3M DP460) to minimize the thickness of the bonding layer. The offset between adjacent piezoelectric patches is 0.1 mm to reduce the stiffness mismatch between the bonded and unbonded areas of the beam. To obtain the dispersion curves of Figs. 3–6, a wideband voltage signal is applied to the last piezoelectric pair to excite the system. The wideband excitation signal is centered at 6500 Hz in Figs. 3–5 and at 5000 Hz in Fig. 6. We use a Polytec PSV-500 scanning laser Doppler vibrometer to measure the out-of-plane velocity of 300 points along the beam. Fast Fourier transformation is applied to the recorded velocity field in space and time to obtain the dispersion curves. Figure 13 shows the measured velocity field along with the input signal and its frequency spectrum corresponding to the results shown in Figs. 3–5, 7, 8.

2. Finite-element model and numerical simulations

We used the commercial finite-element software COMSOL MULTIPHYSICS 5.5 to model the spatiotemporal piezoelectric metamaterial. The model's material properties and size align with those of the experiment. Aluminum 6061 (solid, T6) was chosen from the material library for the central shim, with dimensions of 0.317 75 m in length, 0.745 mm in thickness, and 0.5 cm in width. The shim has a mass density of 2700 kg/m^3, a Young's modulus of 70 GPa, and a Poisson ratio of 0.33. Lead zirconate titanate (PZT-5A) was also selected from the library and applied to 31 piezoelectric pairs with a mass density of 7600 kg/m^3. Solid Mechanics physics includes a damping attribute, with an isotropic loss factor of 0.01, for both the central shim and piezoelectric pairs to

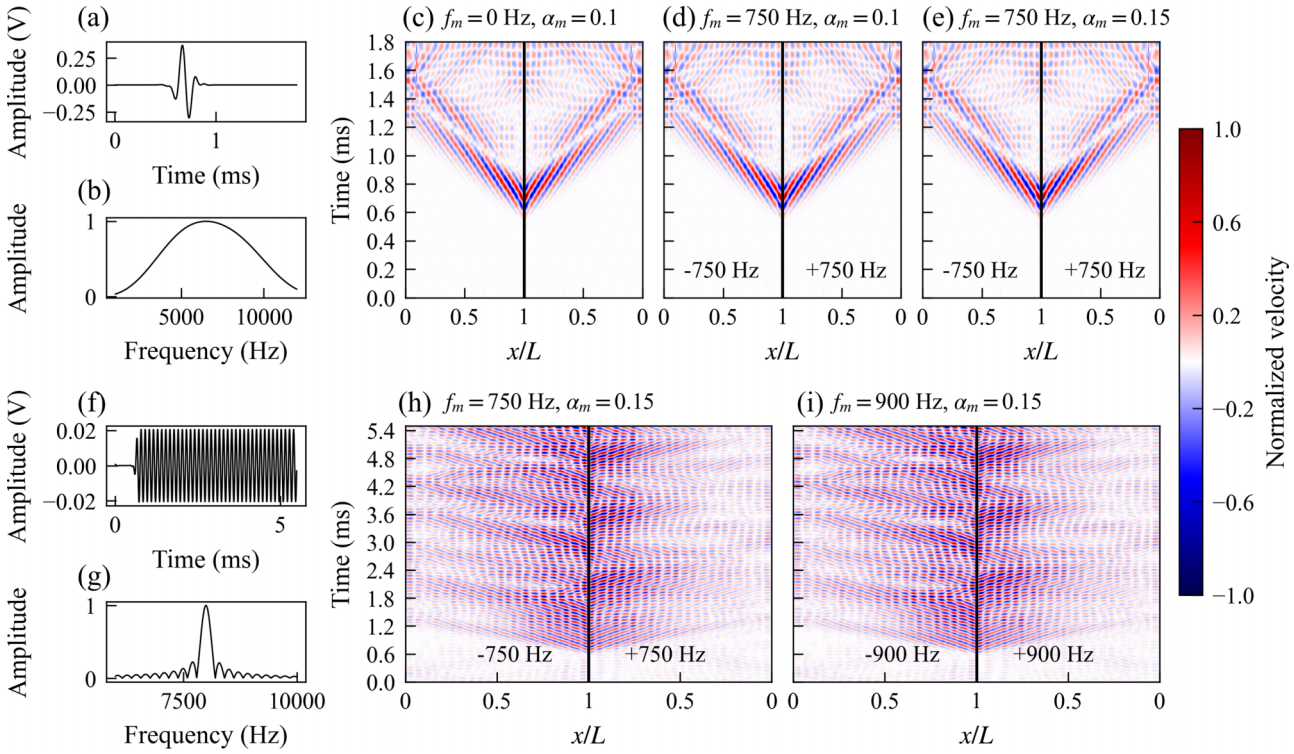

FIG. 13. (a) and (f) Input voltage signal and (b) and (g) the corresponding frequency spectrum. (c)–(e), (h), and (i) Measured out-of-plane velocity under positive and negative modulation frequencies normalized with respect to the largest velocity amplitude of the two cases. Fourier transform of (c), (d), and (e) in space and time yields the dispersion curves of Figs. 3–5, respectively. Fourier transform of (h) and (i) in time yields the frequency spectra of Figs. 7 and 8, respectively.

match the unavoidable damping present in the experimental setup. To reduce the model size, a symmetry boundary was selected, and the left boundary was fixed to simulate the clamped end. A thin elastic layer was added to represent the epoxy layers formed during bonding, with a Young's modulus of 2.3 GPa and a thickness of 0.0432 mm. In Electrostatics physics, the outer surfaces of the central shim were designated as terminals with zero voltage, and 31 separate terminals (of type Circuit) were created, each representing the outer surfaces of a piezoelectric pair. In Electrical Circuit physics, a resistor in series with an inductor was added for each unit cell, with the resistor having a small value of 10 Ω for numerical stability. The inductor value varies in space and time according to the desired parameters. The segregated option is added under the time-dependent solver with two steps to accelerate solution convergence. The model is excited by applying a 2 V peak-to-peak wideband voltage signal centered at 6500 and 5000 Hz across the outer boundaries of the last piezoelectric pair. The resulting out-of-plane velocity field of 200 points along the beam is then exported, and the corresponding dispersion contours are obtained by applying 2D FFT.

[1] J. C. Maxwell, L. on the calculation of the equilibrium and stiffness of frames, London Edinburgh Dublin Philos. Mag. J. Sci. **27**, 294 (1864).

[2] S. Rayleigh, General theorems relating to vibrations: Sec. I. The stationary condition, Sec. II. The dissipation function, Sec. III. A law of reciprocal character, Proc. London Math. Soc **4**, 357 (1873).

[3] R. Fleury, D. Sounas, M. R. Haberman, and A. Alù, Nonreciprocal acoustics, Acoust. Today **11**, 14 (2015).

[4] R. Fleury, M. R. Haberman, G. Huang, and A. N. Norris, Introduction to the special issue on non-reciprocal and topological wave phenomena in acoustics, J. Acoust. Soc. Am. **146**, 719 (2019).

[5] H. Nassar, B. Yousefzadeh, R. Fleury, M. Ruzzene, A. Alù, C. Daraio, A. N. Norris, G. Huang, and M. R. Haberman, Nonreciprocity in acoustic and elastic materials, Nat. Rev. Mater. **5**, 667 (2020).

[6] R. Fleury, D. L. Sounas, C. F. Sieck, M. R. Haberman, and A. Alù, Sound isolation and giant linear nonreciprocity in a compact acoustic circulator, Science **343**, 516 (2014).

[7] T. Ioppolo and P. Rostami, Dispersion and non-reciprocal elastic wave propagation in a membrane coupled with a uniform flow, J. Appl. Phys. **122**, 124902 (2017).

[8] F. Zangeneh-Nejad and R. Fleury, Doppler-based acoustic gyrator, Appl. Sci. **8**, 1083 (2018).

[9] C. P. Wiederhold, D. L. Sounas, and A. Alù, Nonreciprocal acoustic propagation and leaky-wave radiation in a waveguide with flow, J. Acoust. Soc. Am. **146**, 802 (2019).

[10] B. Liang, X. Guo, J. Tu, D. Zhang, and J. Cheng, An acoustic rectifier, Nat. Mater. **9**, 989 (2010).

[11] S. Lepri and A. Pikovsky, Nonreciprocal wave scattering on nonlinear string-coupled oscillators, Chaos **24**, 043119 (2014).
[12] C. Coulais, D. Sounas, and A. Alù, Static non-reciprocity in mechanical metamaterials, Nature (London) **542**, 461 (2017).
[13] J.-G. Cui, T. Yang, and L.-Q. Chen, Frequency-preserved nonreciprocal acoustic propagation in a granular chain, Appl. Phys. Lett. **112**, 181904 (2018).
[14] K. J. Moore, J. Bunyan, S. Tawfick, O. V. Gendelman, S. Li, M. Leamy, and A. F. Vakakis, Nonreciprocity in the dynamics of coupled oscillators with nonlinearity, asymmetry, and scale hierarchy, Phys. Rev. E **97**, 012219 (2018).
[15] B. Luo, S. Gao, J. Liu, Y. Mao, Y. Li, and X. Liu, Non-reciprocal wave propagation in one-dimensional nonlinear periodic structures, AIP Adv. **8**, 015113 (2018).
[16] Z.-N. Li, B. Yuan, Y.-Z. Wang, G.-S. Shui, C. Zhang, and Y.-S. Wang, Diode behavior and nonreciprocal transmission in nonlinear elastic wave metamaterial, Mech. Mater. **133**, 85 (2019).
[17] A. Mojahed, J. Bunyan, S. Tawfick, and A. F. Vakakis, Tunable acoustic nonreciprocity in strongly nonlinear waveguides with asymmetry, Phys. Rev. Appl. **12**, 034033 (2019).
[18] Z. Lu and A. N. Norris, Non-reciprocal wave transmission in a bilinear spring-mass system, J. Vib. Acoust. **142**, 021006 (2020).
[19] B.-I. Popa and S. A. Cummer, Non-reciprocal and highly nonlinear active acoustic metamaterials, Nat. Commun. **5**, 3398 (2014).
[20] G. Librandi, E. Tubaldi, and K. Bertoldi, Programming nonreciprocity and reversibility in multistable mechanical metamaterials, Nat. Commun. **12**, 3454 (2021).
[21] G. U. Patil, S. Cui, and K. H. Matlack, Leveraging nonlinear wave mixing in rough contacts-based phononic diodes for tunable nonreciprocal waves, Extreme Mech. Lett. **55**, 101821 (2022).
[22] R. Fleury, D. L. Sounas, and A. Alù, Subwavelength ultrasonic circulator based on spatiotemporal modulation, Phys. Rev. B **91**, 174306 (2015).
[23] G. Trainiti and M. Ruzzene, Non-reciprocal elastic wave propagation in spatiotemporal periodic structures, New J. Phys. **18**, 083047 (2016).
[24] H. Nassar, H. Chen, A. Norris, M. Haberman, and G. Huang, Non-reciprocal wave propagation in modulated elastic metamaterials, Proc. R. Soc. A **473**, 20170188 (2017).
[25] J. Vila, R. K. Pal, M. Ruzzene, and G. Trainiti, A Bloch-based procedure for dispersion analysis of lattices with periodic time-varying properties, J. Sound Vib. **406**, 363 (2017).
[26] H. Nassar, X. Xu, A. Norris, and G. Huang, Modulated phononic crystals: Non-reciprocal wave propagation and Willis materials, J. Mech. Phys. Solids **101**, 10 (2017).
[27] K. Yi, M. Ouisse, E. Sadoulet-Reboul, and G. Matten, Active metamaterials with broadband controllable stiffness for tunable band gaps and non-reciprocal wave propagation, Smart Mater. Struct. **28**, 065025 (2019).
[28] A. Palermo, P. Celli, B. Yousefzadeh, C. Daraio, and A. Marzani, Surface wave non-reciprocity via time-modulated metamaterials, J. Mech. Phys. Solids **145**, 104181 (2020).
[29] M. Attarzadeh, J. Callanan, and M. Nouh, Experimental observation of nonreciprocal waves in a resonant metamaterial beam, Phys. Rev. Appl. **13**, 021001(R) (2020).
[30] R. Fleury, A. B. Khanikaev, and A. Alù, Floquet topological insulators for sound, Nat. Commun. **7**, 11744 (2016).
[31] N. Geib, A. Sasmal, Z. Wang, Y. Zhai, B.-I. Popa, and K. Grosh, Tunable nonlocal purely active nonreciprocal acoustic media, Phys. Rev. B **103**, 165427 (2021).
[32] Z.-N. Li, Y.-Z. Wang, and Y.-S. Wang, Nonreciprocal phenomenon in nonlinear elastic wave metamaterials with continuous properties, Int. J. Solids Struct. **150**, 125 (2018).
[33] Z. Chen, Y. Peng, H. Li, J. Liu, Y. Ding, B. Liang, X.-F. Zhu, Y. Lu, J. Cheng, and A. Alù, Efficient nonreciprocal mode transitions in spatiotemporally modulated acoustic metamaterials, Sci. Adv. **7**, eabj1198 (2021).
[34] J. Marconi, E. Riva, M. Di Ronco, G. Cazzulani, F. Braghin, and M. Ruzzene, Experimental observation of nonreciprocal band gaps in a space-time-modulated beam using a shunted piezoelectric array, Phys. Rev. Appl. **13**, 031001(R) (2020).
[35] Y. Chen, X. Li, H. Nassar, A. N. Norris, C. Daraio, and G. Huang, Nonreciprocal wave propagation in a continuum-based metamaterial with space-time modulated resonators, Phys. Rev. Appl. **11**, 064052 (2019).
[36] A. Bergamini, T. Delpero, L. D. Simoni, L. D. Lillo, M. Ruzzene, and P. Ermanni, Phononic crystal with adaptive connectivity, Adv. Mater. **26**, 1343 (2014).
[37] B.-I. Popa, D. Shinde, A. Konneker, and S. A. Cummer, Active acoustic metamaterials reconfigurable in real time, Phys. Rev. B **91**, 220303(R) (2015).
[38] Z. Wang, Q. Zhang, K. Zhang, and G. Hu, Tunable digital metamaterial for broadband vibration isolation at low frequency, Adv. Mater. **28**, 9857 (2016).
[39] F. Zangeneh-Nejad and R. Fleury, Active times for acoustic metamaterials, Rev. Phys. **4**, 100031 (2019).
[40] L. Ning, Y.-Z. Wang, and Y.-S. Wang, Active control cloak of the elastic wave metamaterial, Int. J. Solids Struct. **202**, 126 (2020).
[41] C. Sugino, M. Ruzzene, and A. Erturk, Nonreciprocal piezoelectric metamaterial framework and circuit strategies, Phys. Rev. B **102**, 014304 (2020).
[42] Y. Wang, B. Yousefzadeh, H. Chen, H. Nassar, G. Huang, and C. Daraio, Observation of nonreciprocal wave propagation in a dynamic phononic lattice, Phys. Rev. Lett. **121**, 194301 (2018).
[43] J. Nečásek, J. Václavík, and P. Márton, Digital synthetic impedance for application in vibration damping, Rev. Sci. Instrum. **87**, 024704 (2016).
[44] N. Chamanara, S. Taravati, Z.-L. Deck-Léger, and C. Caloz, Optical isolation based on space-time engineered asymmetric photonic band gaps, Phys. Rev. B **96**, 155409 (2017).
[45] Y. Chen, M. Kadic, and M. Wegener, Roton-like acoustical dispersion relations in 3D metamaterials, Nat. Commun. **12**, 3278 (2021).
[46] J. A. Iglesias Martínez, M. F. Groß, Y. Chen, T. Frenzel, V. Laude, M. Kadic, and M. Wegener, Experimental observation of roton-like dispersion relations in metamaterials, Sci. Adv. **7**, eabm2189 (2021).